CHEMISTRY OF MATERIALS

pubs.acs.org/cm

Article

Enhanced Blue Emission in Rb_2HfCl_6 Double Perovskite via Bi^{3+} Doping and Cs^+ Alloying

Haoyue Wan,[▽] Fengyan Jia,[▽] Filip Dinic, Muhammad Imran, Benjamin Rehl, Yanjiang Liu, Watcharaphol Paritmongkol, Pan Xia, Ya-Kun Wang, Yuan Liu, Sasa Wang, Quan Lyu, Giovanni Francesco Cotella, Peter Chun, Oleksandr Voznyy, Sjoerd Hoogland, and Edward H. Sargent*

Cite This: https://doi.org/10.1021/acs.chemmater.2c02673

Read Online

ACCESS | Metrics & More | Article Recommendations | Supporting Information

ABSTRACT: Lead-free double perovskites offer non-toxic properties and strong emission via alloying and doping. Herein, we report the synthesis of Bi-doped pure Rb_2HfCl_6 and Cs-alloyed $RbCsHfCl_6$ microcrystals. The pure Rb_2HfCl_6 microcrystals are nearly non-emissive while alloying with Cs and Bi doping lead to strong deep blue emission at 466 nm with an increase in photoluminescence quantum yield from ∼0 to 66%. Density functional theory studies attest to the improved phase stability due to Cs-alloying and link photoluminescence to Bi^{3+} dopant-induced localized states.

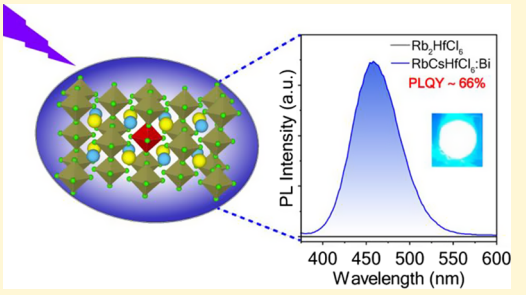

INTRODUCTION

In lead halide perovskites, with their excellent optical and photovoltaic properties,[1−4] the reliance on lead and the question of stability[5−8] motivate the continued investigation of new compositions.[9,10] Among them, vacancy-ordered double perovskite materials with the chemical formula A_2MX_6 have attracted significant attention.[11−13] This family of materials includes a large number of possible compositions, allowing a range of metal cations, halides, and dopants within a given structure.

Several vacancy-ordered double perovskite materials have been reported in recent years. Examples include A_2ZrX_6, A_2SnX_6, and A_2HfX_6 (where A is Cs or Rb and X are Cl, Br, or their mixture). These materials often exhibit weak photoluminescence (PL), with self-trapped excitons modulated via doping and alloying with metal cations. Efficient near-infrared emission in Zr-based double perovskites has been achieved via co-doping Te^{4+} and lanthanide ions.[14] The bandgap of Zr-based double perovskites is further modulated by varying the halide composition.[15] Similarly, bismuth doping in Cs_2SnCl_6 has shown deep-blue emission centered at 455 nm with a photoluminescence quantum yield (PLQY) of ∼80%.[5] A_2HfX_6 is a candidate in the vacancy-ordered perovskite family, potentially useful for light emission and X-ray scintillation, but until now little-explored, with Cs_2HfCl_6 only recently reported.[16] There remain opportunities to investigate material combinations obtained via cation/anion alloying and doping in the context of A_2HfX_6.

RESULTS AND DISCUSSION

We synthesized Rb_2HfCl_6 employing a modified version of a reported method to grow Hf-based perovskites at room temperature.[17] The crystalline structure of Rb_2HfCl_6 was characterized using powder X-ray diffraction (PXRD, Figure S1), which revealed XRD patterns similar to those of Cs_2HfCl_6.[16] This similarity suggests that Rb_2HfCl_6 exhibits the $Fm\bar{3}m$ space group, where the Hf^{4+} ion occupies the center position and coordinates with six Cl^- ions to form $[HfCl_6]^{4-}$ octahedra (Figure S2). The Rb^+ ion is bonded to 12 equivalent Cl^- ions to form $RbCl_{12}$ cuboctahedra, which share facets with 6 other equivalent $RbCl_{12}$ cuboctahedra, 4 equivalent $HfCl_6$ octahedra, and 4 vacant octahedra. The overall structure is that of a vacancy-ordered double perovskite.[10] The grown crystals exhibited a predominantly pyramidal shape with sizes in the 1−10 μm range (Figure 1a).

The emission intensity of Rb_2HfCl_6 under 365 nm excitation was low (Figure S3a), which we attribute to defect states evidenced by two broad absorption features around 300 and 375 nm (Figure 1b).[16] Seeking to enhance the luminescence efficiency, we employed a B-site doping strategy.[18−20] In particular, bismuth is a candidate dopant of interest considering the ns^2 electron configuration[9] and its success in similar materials.[9,21,22] We found Bi-doped materials to be

Received: August 30, 2022
Revised: January 3, 2023
Published: January 17, 2023

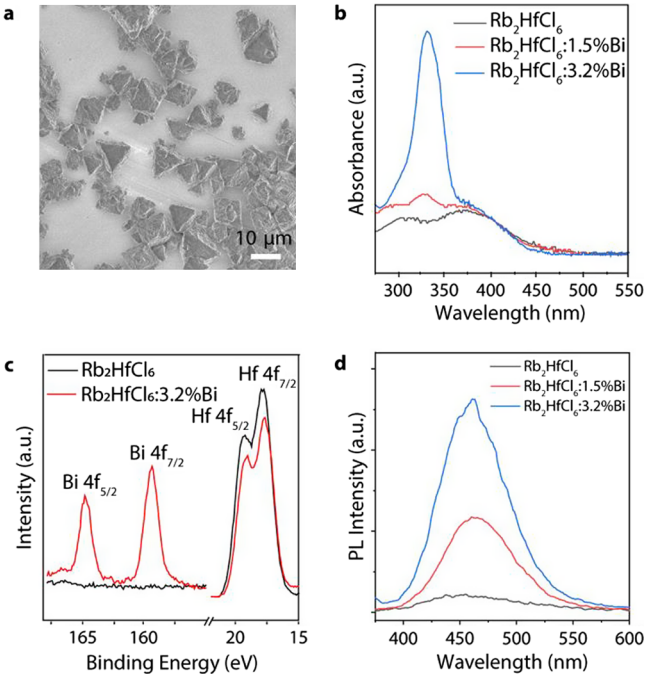

Figure 1. Rb_2HfCl_6 doped with Bi enhances PL. (a) SEM image of Rb_2HfCl_6. (b) Absorption spectra of Rb_2HfCl_6, Rb_2HfCl_6:1.5%Bi, and Rb_2HfCl_6:3.2%Bi. (c) High-resolution Bi 4f and Hf 4f XPS spectra of Rb_2HfCl_6 and Rb_2HfCl_6:3.2%Bi. (d) PL spectra of Rb_2HfCl_6, Rb_2HfCl_6:1.5%Bi, and Rb_2HfCl_6:3.2%Bi under the excitation at 350 nm.

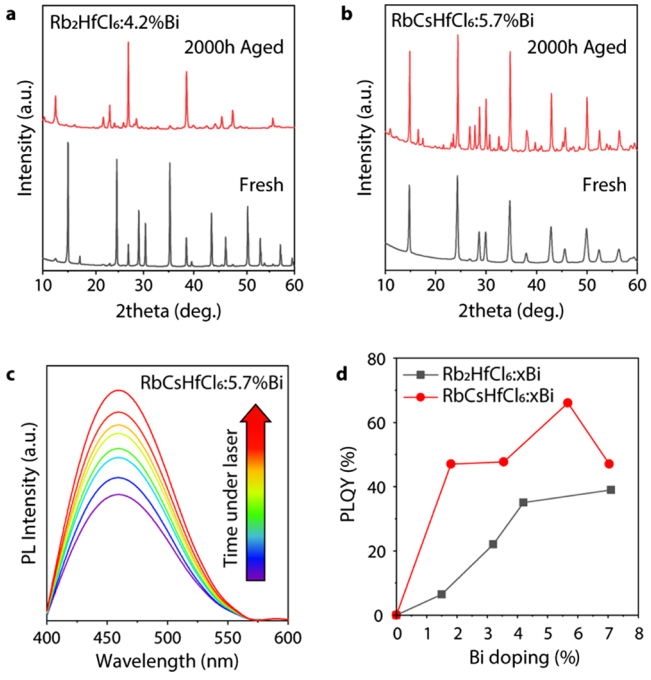

Figure 2. Rb_2HfCl_6:Bi alloyed with Cs stabilizes the material and further enhances PL. (a) XRD patterns of the fresh and aged sample of Rb_2HfCl_6:4.2%Bi. (b) XRD patterns of the fresh and aged sample of $RbCsHfCl_6$:5.7%Bi. (c) PL intensity of $RbCsHfCl_6$:5.7%Bi under intense femtosecond laser excitation over 200 min. (d) PLQY of Rb_2HfCl_6:x%Bi and $RbCsHfCl_6$:x%Bi with varying x.

emissive under excitation using a 365 nm UV lamp (Figure S3b,c). Successful bismuth doping was confirmed via X-ray photoelectron spectroscopy (XPS, Figure 1c) as two peaks at 164.63 and 159.26 eV in the doped perovskite, corresponding to Bi^{3+} $4f_{5/2}$ and $4f_{7/2}$, respectively. Optical absorption spectra showed an additional peak at 330 nm in the doped materials (Figure 1b) that we associated with absorption by the Bi dopant.[5,20,23]

To investigate the photophysical properties of Bi-doped Rb_2HfCl_6, we measured PL and PL excitation (PLE) spectra as a function of doping concentration. Under excitation at 350 nm, the emission peak was centered at 464 nm with a full-width half maximum of 65 nm (Figure 1d). In contrast, samples without bismuth doping showed weaker emissions under the same conditions. While monitoring at 464 nm, the PLE spectrum of Bi-doped Rb_2HfCl_6 displayed a peak at 335 nm (Figure S4), corresponding to absorption by the Bi dopant. The broad emission and large Stokes shift are attributed to self-trapped excitons (STEs).[20,24−27] Due to strong electron−phonon interactions, excitons transfer energy to the lattice and cause lattice distortions. These excited electrons and holes are self-trapped in this distorted lattice and form a stable state. The dissipated energy of the exciton and the change of nuclear coordinates in the lattice distortion lead to the large observed Stokes shift.

We found that Rb_2HfCl_6:Bi was not stable under ambient conditions: as shown in Figure 2a, the XRD features changed significantly after exposure to air for more than 2000 h, indicating a phase change in the material. The XRD peaks of the aged material correspond to those of RbCl crystals (Figure S5), implying that Rb_2HfCl_6 decomposes into RbCl and $HfCl_4$ upon air exposure (Figure S2). We posit that this phase change may arise from the small A-site metallic element, Rb.

We pursued a co-alloying strategy to synthesize $RbCsHfCl_6$:Bi using processes similar to those used for the pure Rb perovskite. The Cs-alloyed crystals showed a smaller crystal size (Figure S6). This Cs-alloyed, Bi-doped perovskite material was stable upon long-term exposure to air, as change indicated by XRD. The intense perovskite diffraction peak at 24° in the aged sample implies that no phase change occurred after 2000 h (Figure 2b). The enhanced stability was also apparent when we subjected $RbCsHfCl_6$:Bi to intense femtosecond laser radiation at 10 mW for over 200 min, which resulted in no degradation of the PL intensity (Figure 2c). Furthermore, the alloyed $RbCsHfCl_6$:Bi perovskite exhibited an improved PLQY. We measured the PLQY of materials with different bismuth doping ratios. As shown in Figure 2d, a maximum PLQY of 66% was achieved for the sample $RbCsHfCl_6$:5.7%Bi, whereas the non-alloyed perovskite material reached a maximum PLQY of 40%.

We then characterized the optical properties of Bi^{3+}-doped $RbCsHfCl_6$ materials. Compared to the material without Bi doping which has two broad absorption peaks centered around 300 and 365 nm, Bi^{3+} doping introduces a narrow peak at 330 nm (Figure 3a). Considering the allowed transition[9,10] in Bi^{3+}, we attribute this peak to the transition $^1S_0 \rightarrow {}^3P_1$.[28−30]

Aiming to understand the origin of the luminescence in the alloyed material, we measured the PL and PLE spectra of doped materials at different excitation and emission wavelengths. While varying the monitored emission wavelength from 410 to 520 nm, the PLE line shape remained similar (Figure 3b).[19,31] Additionally, the PLE spectra showed negligible signals at 400 nm while absorbance was large there (Figure 3a). This implies poor energy transfer between the perovskite host and Bi dopants.[5] The lack of other excitation peaks suggests that Bi is the main contributor to the emission

https://doi.org/10.1021/acs.chemmater.2c02673
Chem. Mater. XXXX, XXX, XXX−XXX

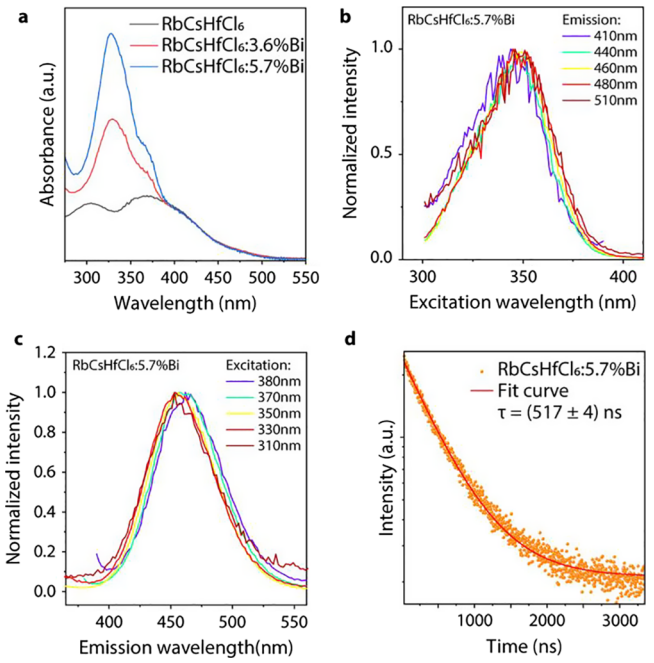

Figure 3. Investigation into the origin of emission from $RbCsHfCl_6$:Bi. (a) Optical absorption spectra of $RbCsHfCl_6$:*x*%Bi at different Bi concentrations (*x* = 0, 3.6, 5.7%). (b) PLE spectra of $RbCsHfCl_6$:5.7%Bi under different monitoring wavelengths. (c) PL spectra of $RbCsHfCl_6$:5.7%Bi under different excitation wavelengths. (d) Time-resolved PL decay curve at 464 nm of $RbCsHfCl_6$:5.7%Bi under 374 nm excitation. The red line is the fitted result from a mono-exponential decay function.

process. Similarly, the emission spectra showed negligible peak shifts when the excitation wavelength varied from 310 to 380 nm (Figure 3c). Without Bi^{3+} doping, there is a weak and broad emission centered at around 480 nm that is obtained only upon excitation below 300 nm (Figure S7), consistent with Bi contributing to the observed high-efficiency emission. We posit that the emission originates from either the Bi^{3+} ions or the interactions between STEs and the Bi^{3+} ions.[23] Yet, the wide peak width for both the excitation and emission spectra argues against Bi^{3+} ionoluminescence.[5,23,32] Therefore, considering the large Stokes shift and broad emission peak width, we conclude that the origin of the PL emission is the Bi^{3+}-induced STEs.[16,20]

Transient PL (TRPL) measurements were carried out for a deeper understanding of the luminescence mechanism. The TRPL decay curve of $RbCsHfCl_6$:5.7%Bi measured at 464 nm with a 374 nm excitation laser can be fitted with a mono-exponential decay function (Figure 3d). The fit result reveals an emission lifetime of 517 ± 4 ns, which is in agreement with previous reports on double perovskite systems.[15,33,34] TRPL decay curves at emission wavelengths varying from 410 to 510 nm showed a similar emission lifetime (Figure S8). These short PL lifetimes further argue against emission from the host in light of the extremely long lifetime of the host STEs[35−38] and support emission originating from singlet dopant STEs[20] rather than from common STEs[17,36] that emit in the order of several microseconds.

To gain insight into the effect of Bi doping on the band structure of Rb_2HfCl_6, we performed density functional theory (DFT) simulations. The calculations revealed that Bi creates new states near the valence band, whereas the higher-lying Bi orbitals remain within the conduction band, even with the inclusion of spin−orbit coupling (Figure 4a,b). The wave-

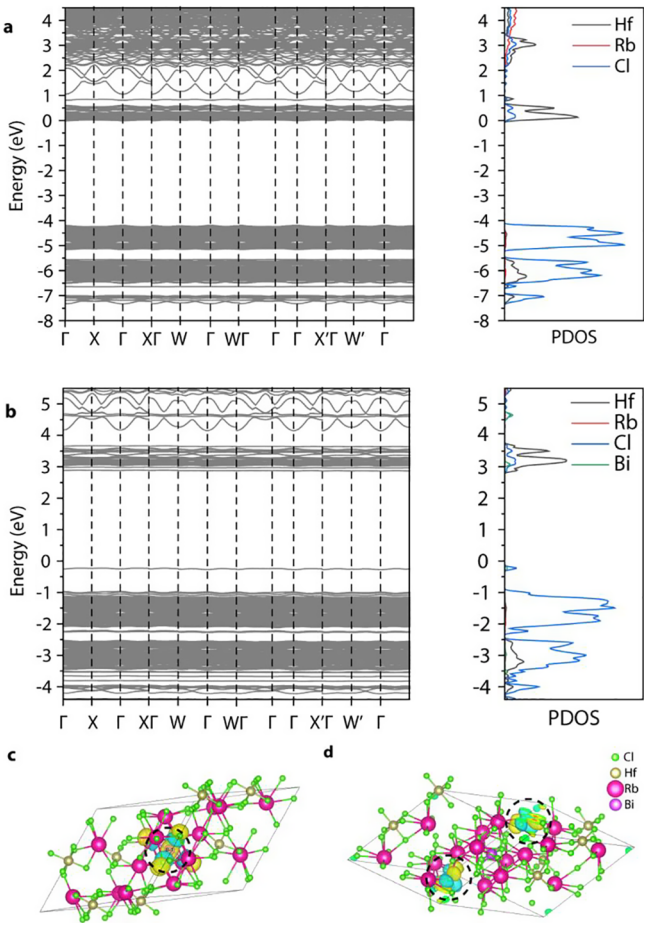

Figure 4. DFT studies. (a, b) Band structures and projected densities of states for Rb_2HfCl_6 without and with Bi doping. (c, d) Valence band and conduction band wavefunctions for Rb_2HfCl_6 with Bi doping.

functions show new states near the valence band strongly localized on Bi (Figure 4c), accounting for the enhanced brightness of the exciton. The conduction band remains delocalized over the entire crystal, primarily on Hf atoms (Figure 4d).

DFT was also used to explore the instability and phase decomposition of Rb_2HfCl_6 and its improvement with Cs alloying. We found that at 0 K, the Rb-based crystal is 0.1 eV/atom more stable relative to RbCl and $HfCl_4$ precursors, and stability improves to 0.16 eV/atom for the Cs-based crystal. The lower stability of Rb-based crystals is in line with the smaller size of Rb ions, which is a common problem for perovskite-like crystals. While the calculation predicts that Rb_2HfCl_6 should remain phase-stable at 0 K, this stability may change at room temperature since entropic effects are known to be quite strong in perovskites. For example, entropy contribution is responsible for phase conversion (e.g., $CsPbI_3$) upon heating.[39] To account for this entropic effect, we performed molecular dynamics simulations at room temperature on all crystal phases involved. We found that the stability difference increases to 0.4 eV/atom for Rb versions vs the Cs counterparts.

https://doi.org/10.1021/acs.chemmater.2c02673
Chem. Mater. XXXX, XXX, XXX−XXX

In summary, we synthesized a lead-free double perovskite exhibiting deep blue luminescence at 466 nm with a quantum efficiency of 66%. Although the host crystal, Rb_2HfCl_6, was non-emissive under excitation above 300 nm, bismuth doping improved the luminescence and excitation range. Cs-alloying improved the stability, as evidenced by the retention of the native structural features following 2000 h of aging. Spectroscopic analysis indicates that light emission from Bi-doped and Cs-alloyed materials originates from Bi-induced STEs, rather than Bi^{3+} ionoluminescence. Through DFT, we found valence band states localized near bismuth ions that may account for the enhanced exciton brightness compared to the case of the undoped material. DFT also showed an increase in stability for the Cs-based crystal compared to the Rb-based crystal.

EXPERIMENTAL SECTION

Materials. Cesium chloride (CsCl, ReagentPlus, 99.9%, Sigma-Aldrich), hafnium(IV) chloride ($HfCl_4$, 98%, Sigma-Aldrich), bismuth(III) chloride ($BiCl_3$, reagent grade, ≥98%, Sigma-Aldrich), and hydrochloric acid (ACS reagent, 37%, Sigma-Aldrich) were purchased from Sigma-Aldrich. Rubidium chloride (RbCl, 99.8%-Rb) was purchased from Strem Chemicals. All chemicals were used as received.

Synthesis of $Rb_xCs_{2-x}HfCl_6$:Bi_y. First, x mmol of RbCl and $2 - x$ mmol of CsCl were dissolved in 6 mL of 37% HCl solution. Meanwhile, y mmol of $BiCl_3$ and $1 - y$ mmol of $HfCl_4$ were dissolved in 10 mL of 37% HCl solution in a 50 mL plastic falcon tube. Then, the first solution was dripped into the second mixture, and a white precipitate appeared in the solution immediately. After reaction completion, the suspension was centrifuged at 7800 rpm to remove unreacted precursors. The supernatant was discarded, and the precipitation was washed with isopropanol four times. The final product was obtained after drying in an oven at 50 °C.

Absorption Measurements. Crystals were first dispersed in isopropanol to form a suspension. Samples were created by dropping the suspension on a glass substrate and drying. Absorption spectra were collected with a Perkin Elmer 950 UV−vis−NIR spectrometer equipped with an integrating sphere for film measurements.

Scanning Electron Microscopy. The morphologies of the samples were investigated using SEM on a Hitachi SU-8230 apparatus with an acceleration voltage of 1 kV.

Powder X-ray Diffraction Measurements. Powder X-ray diffraction was recorded using a Rigaku MiniFlex 600 6G benchtop powder X-ray diffractometer with a NaI scintillation counter and a monochromatized Cu Kα radiation source (λ = 1.5406 Å) operating at a voltage of 40 kV and current of 15 mA.

Photoluminescence Measurements. Samples were created in the same way as absorption measurements. PL spectra were collected using a Horiba Fluorolog system with a calibrated monochromator and a time-correlated single photon counting detector. For steady-state PL measurements, a xenon lamp was used as the excitation source. For time-resolved PL, a 374 nm laser diode was used with the overall time resolution of Δt = 0.13 ns limited by the instrument response function.

PLQY Measurements. PLQY measurements were done using a Quanta-Phi integrating sphere coupled to a Horiba Fluorolog system with optical fiber bundles. A monochromated xenon lamp was used as the excitation source. The Fluorolog was set to an excitation wavelength of 350 nm and to a 5 nm bandpass for both the excitation and emission slits. The detector and integrating sphere were corrected for spectral variance using a Newport calibrated white light source. The PLQY was calibrated using standard materials with known PLQY values and emission covering the measurement range, including Coumarin 6, Coumarin 153, and Rhodamine 6G.

XPS Measurements. X-ray Photoelectron Spectroscopy Measurements: X-ray photoelectron spectroscopy measurements were carried out on a Thermofisher Scientific K-Alpha spectrometer, using Al Kα X-ray radiation (1486.6 eV) for excitation.

DFT Calculations. Geometry optimization, energy calculations, and molecular dynamics calculations were performed using the Vienna ab initio simulation package[40,41] employing a plane wave basis set with the Perdew−Burke−Ernzerhof[42] functional. The projector-augmented wave method[43] was used to solve the ion−electron interactions in the periodic system. The Monkhorst-Pack k-points mesh with a Kmesh-resolved value of 0.04 2π/Angstroms was utilized.[44] The MD calculation was run at 293 Kelvin, with a 0.5 fs time step. The band structure and PDOS were calculated utilizing spin−orbit coupling.[45]

ASSOCIATED CONTENT

Supporting Information

The Supporting Information is available free of charge at https://pubs.acs.org/doi/10.1021/acs.chemmater.2c02673.

XRD patterns, crystal structure, luminescence photos, optical spectra, and SEM images (PDF)

AUTHOR INFORMATION

Corresponding Author

Edward H. Sargent − *Department of Electrical and Computer Engineering, University of Toronto, Toronto, Ontario M5S 3G4, Canada;* orcid.org/0000-0003-0396-6495; Email: ted.sargent@utoronto.ca

Authors

Haoyue Wan − *Department of Electrical and Computer Engineering, University of Toronto, Toronto, Ontario M5S 3G4, Canada;* orcid.org/0000-0001-8137-9152

Fengyan Jia − *Department of Electrical and Computer Engineering, University of Toronto, Toronto, Ontario M5S 3G4, Canada; Beijing National Laboratory for Molecular Sciences, State Key Laboratory of Rare Earth Materials Chemistry and Applications, PKU-HKU Joint Laboratory in Rare Earth Materials and Bioinorganic Chemistry, College of Chemistry and Molecular Engineering, Peking University, Beijing 100871, China*

Filip Dinic − *Department of Physical and Environmental Sciences, University of Toronto, Toronto, Ontario M1C 1A4, Canada*

Muhammad Imran − *Department of Electrical and Computer Engineering, University of Toronto, Toronto, Ontario M5S 3G4, Canada;* orcid.org/0000-0001-7091-6514

Benjamin Rehl − *Department of Electrical and Computer Engineering, University of Toronto, Toronto, Ontario M5S 3G4, Canada*

Yanjiang Liu − *Department of Electrical and Computer Engineering, University of Toronto, Toronto, Ontario M5S 3G4, Canada;* orcid.org/0000-0002-6119-2793

Watcharaphol Paritmongkol − *Department of Electrical and Computer Engineering, University of Toronto, Toronto, Ontario M5S 3G4, Canada;* orcid.org/0000-0003-1638-6828

Pan Xia − *Department of Electrical and Computer Engineering, University of Toronto, Toronto, Ontario M5S 3G4, Canada*

Ya-Kun Wang − *Department of Electrical and Computer Engineering, University of Toronto, Toronto, Ontario M5S 3G4, Canada*

Yuan Liu − *Department of Electrical and Computer Engineering, University of Toronto, Toronto, Ontario M5S 3G4, Canada;* orcid.org/0000-0001-8611-1673

Sasa Wang − *Department of Electrical and Computer Engineering, University of Toronto, Toronto, Ontario M5S 3G4, Canada*
Quan Lyu − *Huawei Technologies Research and Development (UK) Ltd., Cambridge CB4 0FY, U. K.*
Giovanni Francesco Cotella − *Huawei Technologies Research and Development (UK) Ltd., Ipswich IP5 3RE, U. K.*
Peter Chun − *Huawei Technologies Canada, Markham, Ontario L3R 5A4, Canada*
Oleksandr Voznyy − *Department of Physical and Environmental Sciences, University of Toronto, Toronto, Ontario M1C 1A4, Canada;* orcid.org/0000-0002-8656-5074
Sjoerd Hoogland − *Department of Electrical and Computer Engineering, University of Toronto, Toronto, Ontario M5S 3G4, Canada;* orcid.org/0000-0002-3099-585X

Complete contact information is available at: https://pubs.acs.org/10.1021/acs.chemmater.2c02673

Author Contributions

[▽]H.W. and F.J. contributed equally to this work.

Notes

The authors declare no competing financial interest.

■ ACKNOWLEDGMENTS

This publication is based in part on work supported by the Natural Sciences and Engineering Research Council of Canada (NSERC). The authors also acknowledge Huawei Canada for their financial support. Computations were performed on the Niagra[46] supercomputer at the SciNet HPC Consortium.[47] SciNet is funded by the Canada Foundation for Innovation; the Government of Ontario; Ontario Research Fund − Research Excellence; and the University of Toronto.

■ REFERENCES

(1) Lin, K.; Xing, J.; Quan, L. N.; De Arquer, F.; Gong, X.; Lu, J.; Xie, L.; Zhao, W.; Zhang, D.; Yan, C. Perovskite light-emitting diodes with external quantum efficiency exceeding 20 per cent. *Nature* **2018**, *562*, 245−248.
(2) Cho, H.; Jeong, S.-H.; Park, M.-H.; Kim, Y.-H.; Wolf, C.; Lee, C.-L.; Heo, J. H.; Sadhanala, A.; Myoung, N.; Yoo, S.; Im, S. H.; Friend, R. H.; Lee, T. W. Overcoming the electroluminescence efficiency limitations of perovskite light-emitting diodes. *Science* **2015**, *350*, 1222−1225.
(3) Burschka, J.; Pellet, N.; Moon, S.-J.; Humphry-Baker, R.; Gao, P.; Nazeeruddin, M. K.; Grätzel, M. Sequential deposition as a route to high-performance perovskite-sensitized solar cells. *Nature* **2013**, *499*, 316−319.
(4) Lee, M. M.; Teuscher, J.; Miyasaka, T.; Murakami, T. N.; Snaith, H. J. Efficient hybrid solar cells based on meso-superstructured organometal halide perovskites. *Science* **2012**, *338*, 643−647.
(5) Tan, Z.; Li, J.; Zhang, C.; Li, Z.; Hu, Q.; Xiao, Z.; Kamiya, T.; Hosono, H.; Niu, G.; Lifshitz, E.; Cheng, Y.; Tang, J. Highly Efficient Blue-Emitting Bi-Doped Cs_2SnCl_6 Perovskite Variant: Photoluminescence Induced by Impurity Doping. *Adv. Funct. Mater.* **2018**, *28*, No. 1801131.
(6) Yang, B.; Hong, F.; Chen, J.; Tang, Y.; Yang, L.; Sang, Y.; Xia, X.; Guo, J.; He, H.; Yang, S.; Deng, W.; Han, K. Colloidal Synthesis and Charge-Carrier Dynamics of $Cs_2AgSb_{1-y}Bi_yX_6$ (X: Br, Cl; $0 \leq y \leq 1$) Double Perovskite Nanocrystals. *Angew. Chem. Int. Ed.* **2019**, *131*, 2300−2305.
(7) Kamat, P. V.; Bisquert, J.; Buriak, J. Lead-free perovskite solar cells. *ACS Energy Lett.* **2017**, *2*, 904−905.
(8) Nair, S.; Patel, S. B.; Gohel, J. V. Recent trends in efficiency-stability improvement in perovskite solar cells. *Mater. Today Energy* **2020**, *17*, No. 100449.
(9) Arfin, H.; Kshirsagar, A. S.; Kaur, J.; Mondal, B.; Xia, Z.; Chakraborty, S.; Nag, A. ns^2 Electron (Bi^{3+} and Sb^{3+}) Doping in Lead-Free Metal Halide Perovskite Derivatives. *Chem. Mater.* **2020**, *32*, 10255−10267.
(10) Maughan, A. E.; Ganose, A. M.; Scanlon, D. O.; Neilson, J. R. Perspectives and Design Principles of Vacancy-Ordered Double Perovskite Halide Semiconductors. *Chem. Mater.* **2019**, *31*, 1184−1195.
(11) Saparov, B.; Sun, J.-P.; Meng, W.; Xiao, Z.; Duan, H.-S.; Gunawan, O.; Shin, D.; Hill, I. G.; Yan, Y.; Mitzi, D. B. Thin-film deposition and characterization of a Sn-deficient perovskite derivative Cs_2SnI_6. *Chem. Mater.* **2016**, *28*, 2315−2322.
(12) Kaltzoglou, A.; Antoniadou, M.; Kontos, A. G.; Stoumpos, C. C.; Perganti, D.; Siranidi, E.; Raptis, V.; Trohidou, K.; Psycharis, V.; Kanatzidis, M. G.; Falaras, P. Optical-vibrational properties of the Cs_2SnX_6 (X= Cl, Br, I) defect perovskites and hole-transport efficiency in dye-sensitized solar cells. *J. Phys. Chem. C* **2016**, *120*, 11777−11785.
(13) Maughan, A. E.; Ganose, A. M.; Bordelon, M. M.; Miller, E. M.; Scanlon, D. O.; Neilson, J. R. Defect tolerance to intolerance in the vacancy-ordered double perovskite semiconductors Cs_2SnI_6 and Cs_2TeI_6. *J. Am. Chem. Soc.* **2016**, *138*, 8453−8464.
(14) Sun, J.; Zheng, W.; Huang, P.; Zhang, M.; Zhang, W.; Deng, Z.; Yu, S.; Jin, M.; Chen, X. Efficient Near-Infrared Luminescence in Lanthanide-Doped Vacancy-Ordered Double Perovskite Cs_2ZrCl_6 Phosphors via Te^{4+} Sensitization. *Angew. Chem. Int. Ed.* **2022**, *61*, No. e202201993.
(15) Zheng, K.; Chen, B.; Xie, L.; Li, X.; Lu, B.; Wang, M.; Wu, Y.; Jiang, T.; Zhang, F.; Li, X.; et al. Vacancy-Ordered Double Perovskite $Rb_2ZrCl_{6-x}Br_x$: Facile Synthesis and Insight into Efficient Intrinsic Self-Trapped Emission. *Adv. Opt. Mater.* **2022**, *10*, No. 2101661.
(16) Liu, S.; Yang, B.; Chen, J.; Zheng, D.; Tang, Z.; Deng, W.; Han, K. Colloidal Synthesis and Tunable Multicolor Emission of Vacancy-Ordered Cs_2HfCl_6 Perovskite Nanocrystals. *Laser Photonics Rev.* **2022**, *16*, No. 2100439.
(17) Liu, R.; Zhang, W.; Liu, W.; Li, G. Synthesis of a Bi^{3+}-Doped Cs_2HfCl_6 Double Perovskite with Highly Efficient Blue Light Emission at Room Temperature. *Inorg. Chem.* **2021**, *60*, 10451−10458.
(18) Luo, J.; Wang, X.; Li, S.; Liu, J.; Guo, Y.; Niu, G.; Yao, L.; Fu, Y.; Gao, L.; Dong, Q.; et al. Efficient and stable emission of warm-white light from lead-free halide double perovskites. *Nature* **2018**, *563*, 541−545.
(19) Zeng, R.; Zhang, L.; Xue, Y.; Ke, B.; Zhao, Z.; Huang, D.; Wei, Q.; Zhou, W.; Zou, B. Highly Efficient Blue Emission from Self-Trapped Excitons in Stable Sb^{3+}-Doped $Cs_2NaInCl_6$ Double Perovskites. *J. Phys. Chem. Lett.* **2020**, *11*, 2053−2061.
(20) Chen, B.; Guo, Y.; Wang, Y.; Liu, Z.; Wei, Q.; Wang, S.; Rogach, A. L.; Xing, G.; Shi, P.; Wang, F. Multiexcitonic Emission in Zero-Dimensional Cs_2ZrCl_6:Sb^{3+} Perovskite Crystals. *J. Am. Chem. Soc.* **2021**, *143*, 17599−17606.
(21) Sharma, M.; Yangui, A.; Whiteside, V. R.; Sellers, I. R.; Han, D.; Chen, S.; Du, M.-H.; Saparov, B. $Rb_4Ag_2BiBr_9$: A Lead-Free Visible Light Absorbing Halide Semiconductor with Improved Stability. *Inorg. Chem.* **2019**, *58*, 4446−4455.
(22) Kang, F.; Zhang, Y.; Peng, M. Controlling the Energy Transfer via Multi Luminescent Centers to Achieve White Light/Tunable Emissions in a Single-Phased X2-Type Y_2SiO_5:Eu^{3+},Bi^{3+} Phosphor For Ultraviolet Converted LEDs. *Inorg. Chem.* **2015**, *54*, 1462−1473.
(23) Xiong, G.; Yuan, L.; Jin, Y.; Wu, H.; Li, Z.; Qu, B.; Ju, G.; Chen, L.; Yang, S.; Hu, Y. Aliovalent Doping and Surface Grafting Enable Efficient and Stable Lead-Free Blue-Emitting Perovskite Derivative. *Adv. Opt. Mater.* **2020**, *8*, No. 2000779.
(24) Kowalczyk, T.; Tsuchimochi, T.; Chen, P.-T.; Top, L.; Voorhis, T. V. Excitation energies and Stokes shifts from a restricted open-shell Kohn-Sham approach. *J. Chem. Phys.* **2013**, *138*, No. 164101.

(25) Quan, L. N.; Garcia de Arquer, F. P.; Sabatini, R. P.; Sargent, E. H. Perovskites for Light Emission. *Adv. Mater.* **2018**, *30*, No. e1801996.
(26) Buizza, L. R. V.; Herz, L. M. Polarons and Charge Localization in Metal-Halide Semiconductors for Photovoltaic and Light-Emitting Devices. *Adv. Mater.* **2021**, *33*, No. 2007057.
(27) Paritmongkol, W.; Powers, E. R.; Dahod, N. S.; Tisdale, W. A. Two Origins of Broadband Emission in Multilayered 2D Lead Iodide Perovskites. *J. Phys. Chem. Lett.* **2020**, *11*, 8565−8572.
(28) Yadav, R.; Kumar, D.; Singh, A.; Rai, E.; Rai, S. Effect of Bi^{3+} ion on upconversion-based induced optical heating and temperature sensing characteristics in the Er^{3+}/Yb^{3+} co-doped La_2O_3 nano-phosphor. *RSC Adv.* **2018**, *8*, 34699−34711.
(29) Yadav, R. S.; Rai, S. B. Surface analysis and enhanced photoluminescence via Bi^{3+} doping in a Tb^{3+} doped Y_2O_3 nano-phosphor under UV excitation. *J. Alloys Compd.* **2017**, *700*, 228−237.
(30) Yadav, R. S.; Dhoble, S. J.; Rai, S. B. Improved photon upconversion photoluminescence and intrinsic optical bistability from a rare earth co-doped lanthanum oxide phosphor via Bi^{3+} doping. *New J. Chem.* **2018**, *42*, 7272−7282.
(31) Han, P.; Zhang, X.; Mao, X.; Yang, B.; Yang, S.; Feng, Z.; Wei, D.; Deng, W.; Pullerits, T.; Han, K. Size effect of lead-free halide double perovskite on luminescence property. *Sci. China Chem.* **2019**, *62*, 1405−1413.
(32) Li, S.; Luo, J.; Liu, J.; Tang, J. Self-Trapped Excitons in All-Inorganic Halide Perovskites: Fundamentals, Status, and Potential Applications. *J. Phys. Chem. Lett.* **2019**, *10*, 1999−2007.
(33) Zhang, H.; Zhu, L.; Cheng, J.; Chen, L.; Liu, C.; Yuan, S. Photoluminescence Characteristics of Sn^{2+} and Ce^{3+}-Doped Cs_2SnCl_6 Double-Perovskite Crystals. *Materials* **2019**, *12*, 1501.
(34) Kang, F.; Yang, X.; Peng, M.; Wondraczek, L.; Ma, Z.; Zhang, Q.; Qiu, J. Red Photoluminescence from $Bi^{3+}$and the Influence of the Oxygen-Vacancy Perturbation in $ScVO_4$: A Combined Experimental and Theoretical Study. *J. Phys. Chem. C* **2014**, *118*, 7515−7522.
(35) Zeng, R.; Bai, K.; Wei, Q.; Chang, T.; Yan, J.; Ke, B.; Huang, J.; Wang, L.; Zhou, W.; Cao, S.; et al. Boosting triplet self-trapped exciton emission in Te(IV)-doped Cs_2SnCl_6 perovskite variants. *Nano Res.* **2021**, *14*, 1551−1558.
(36) Chang, T.; Wei, Q.; Zeng, R.; Cao, S.; Zhao, J.; Zou, B. Efficient Energy Transfer in Te^{4+}-Doped Cs_2ZrCl_6 Vacancy-Ordered Perovskites and Ultrahigh Moisture Stability via A-Site Rb-Alloying Strategy. *J. Phys. Chem. Lett.* **2021**, *12*, 1829−1837.
(37) Liu, S.; Yang, B.; Chen, J.; Wei, D.; Zheng, D.; Kong, Q.; Deng, W.; Han, K. Efficient Thermally Activated Delayed Fluorescence from All-Inorganic Cesium Zirconium Halide Perovskite Nanocrystals. *Angew. Chem. Int. Ed.* **2020**, *59*, 21925−21929.
(38) Wei, J.-H.; Liao, J.-F.; Zhou, L.; Luo, J.-B.; Wang, X.-D.; Kuang, D.-B. Indium-antimony-halide single crystals for high-efficiency white-light emission and anti-counterfeiting. *Sci. Adv.* **2021**, *7*, No. eabg3989.
(39) Dastidar, S.; Hawley, C. J.; Dillon, A. D.; Gutierrez-Perez, A. D.; Spanier, J. E.; Fafarman, A. T. Quantitative Phase-Change Thermodynamics and Metastability of Perovskite-Phase Cesium Lead Iodide. *J. Phys. Chem. Lett.* **2017**, *8*, 1278−1282.
(40) Kresse, G.; Furthmüller, J. Efficiency of ab-initio total energy calculations for metals and semiconductors using a plane-wave basis set. *Comput. Mater. Sci.* **1996**, *6*, 15−50.
(41) Kresse, G.; Hafner, J. *Ab initio* molecular dynamics for liquid metals. *Phys. Rev. B* **1993**, *47*, 558−561.
(42) Perdew, J. P.; Burke, K.; Ernzerhof, M. Generalized Gradient Approximation Made Simple. *Phys. Rev. Lett.* **1996**, *77*, 3865−3868.
(43) Payne, M. C.; Teter, M. P.; Allan, D. C.; Arias, T. A.; Joannopoulos, J. D. Iterative minimization techniques for *ab initio* total-energy calculations: molecular dynamics and conjugate gradients. *Rev. Mod. Phys.* **1992**, *64*, 1045−1097.
(44) Monkhorst, H. J.; Pack, J. D. Special points for Brillouin-zone integrations. *Phys. Rev. B* **1976**, *13*, 5188−5192.
(45) Steiner, S.; Khmelevskyi, S.; Marsmann, M.; Kresse, G. Calculation of the magnetic anisotropy with projected-augmented-wave methodology and the case study of disordered $Fe_{1-x}Co_x$ alloys. *Phys. Rev. B* **2016**, *93*, No. 224425.
(46) Ponce, M.; van Zon, R.; Northrup, S.; Gruner, D.; Chen, J.; Ertinaz, F.; Fedoseev, A.; Groer, L.; Mao, F.; Mundim, B. C.; et al.Deploying a Top-100 Supercomputer for Large Parallel Workloads: the Niagara Supercomputer. In *Proceedings of the Practice and Experience in Advanced Research Computing on Rise of the Machines (learning)*, Chicago, IL, USA, 2019/07/28; pp. 1−8.
(47) Loken, C.; Gruner, D.; Groer, L.; Peltier, R.; Bunn, N.; Craig, M.; Henriques, T.; Dempsey, J.; Yu, C.-H.; Chen, J.; et al. SciNet: Lessons Learned from Building a Power-efficient Top-20 System and Data Centre. *J. Phys.: Conf. Ser.* **2010**, *256*, No. 012026.

https://doi.org/10.1021/acs.chemmater.2c02673
Chem. Mater. XXXX, XXX, XXX−XXX